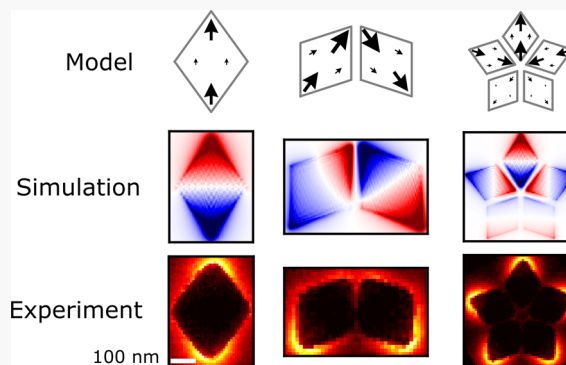Article

Plasmon Hybridization in Nanorhombus Assemblies

Claire A. West,[⊥] Agust Olafsson,[⊥] Grace Pakeltis, David A. Garfinkel, Philip D. Rack, David J. Masiello, Jon P. Camden, and Juan Carlos Idrobo*

Read Online

ACCESS | Metrics & More | Article Recommendations

ABSTRACT: Understanding resonant coupling in plasmonic nano-assemblies is a challenging scientific endeavor, especially for particles with complex nanoarchitectures. Our ability to both model and measure this optical behavior, however, has rapidly developed in the last 20 years via a confluence of fabrication, spectroscopy, and theoretical analysis. Here, we precisely nanofabricate, characterize, and model the coupling and infrared optical responses of different plasmonic nanorhombus assemblies. Ranging from a monomer to a pentamer ensemble, experimental and simulated point spectra, spectrum images, and near-field maps agree well with the results of an analytical coupled normal mode model developed here. The analytical model reveals that the infrared optical responses of the nanorhombus systems can be explained by the coupling of the major and minor axis dipole and a quadrupole localized surface plasmon modes arising from the individual nanorhombus monomers. This model can be used to predict the plasmonic behavior of more complicated systems, and it elucidates the role that short-, intermediate-, and far-field coupling effects play in extended plasmonic assemblies more generally. This work also highlights how localized electron probes in the new generation of monochromated aberration-corrected scanning transmission electron microscopes can be used to study the optical responses of nanofabricated assemblies in the infrared spectral regime.

INTRODUCTION

Over the past several decades, significant effort has been invested to characterize the localized surface plasmon (LSP) resonances in noble metal nanoparticle assemblies.[1−4] LSP resonances are geometry-specific collective oscillations of the free conduction band electrons in a metal. They offer the unique ability to capture far-field light and convert it to intense surface-bound electric fields, effectively focusing light in systems below the diffraction limit.[5,6] There have been numerous studies demonstrating the high sensitivity of the LSP to its local environment, including the nanoparticle shape,[7] proximity to other particles,[8] substrate,[9,10] and other chemical and physical aspects of the system.[11,12] Each of these considerations, however, also presents an opportunity to control the LSP energy, typically in the near-infrared to ultraviolet range, making LSPs excellent candidates for use in biological/chemical sensing,[13,14] waveguiding,[15] catalysis,[16,17] and optoelectronic devices.[18,19]

The unique optical properties of nanoparticle assemblies are determined by the coupled and hybridized LSPs of the individual particles that comprise the assembly.[5,6] Many studies have examined how interparticle LSP coupling is affected by varying the particle size,[20] particle shape,[21] interparticle distance,[22] and environment.[23−26] These analyses are often limited to ensemble material properties because

diffraction-limited optical methods are unable to resolve nanometer-scale phenomena. Near-field optical scanning microscopy[27−29] and scanning transmission electron microscopy (STEM),[30−32] however, have the ability to study the long- and short-range coupling of LSP modes with both nanometer spatial resolution and high energy resolution. Yet even with these techniques, most of the studies have been concentrated on nanostructures that have simple geometries such as spheres, disks, and rods because their plasmonic properties are easier to interpret and model.

In this article, we use high spatial and energy resolution in monochromated aberration-corrected STEM, combined with theoretical modeling, to study the evolution of plasmon coupling in nanostructures with more complex geometries. Using electron energy-loss spectroscopy (EELS) in STEM, we identify the spatial and energy profile of a single plasmonic nanorhombus and study the LSP evolution as more nano-rhombi couple to it. Using this approach, we also develop a
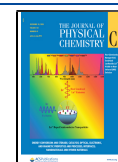
theoretical model based on the normal modes of coupled dipoles to study and predict the LSP hybridization profiles of coupled assemblies. This simplified model not only allows for the interpretation of both the experimental and simulated results presented herein but also lays the foundation for understanding plasmonic coupling in much larger plasmonic assemblies that are not computationally tractable with standard numerical Maxwell equation solvers.

METHODS

Experimental Fabrication/Characterization. The deconstructed rhombuses are fabricated via electron-beam lithography (JEOL 9300FS) using a lift-off process. A 300 μm Si wafer with 30 nm of low-pressure chemical vapor-deposited SiN_x is spin-coated with PMMA 495 A4 and exposed. The pattern is then developed using methyl isobutyl ketone/isopropyl alcohol (IPA) (1:3). Au (25 nm) is sputter-deposited via DC magnetron sputtering onto the substrate, followed by soaking in a heated nuclear microprobe (NMP) bath, sonicating in NMP and acetone, and rinsing with IPA and deionized water. The backside of the wafer is then spin-coated with P20 and S1818 and exposed using photolithography to create the windows of TEM. Reactive ion etching is used to remove the backside nitride layer and the wafer is subsequently submerged in a heated KOH bath to etch the Si windows and TEM grid edges.

Experimental STEM−EELS. EEL spectra in the infrared regime were collected using a Nion aberration-corrected high energy resolution monochromated EELS−STEM (Nion HERMES) operating at a 60 kV accelerating voltage. Point spectra and spectrum images were collected with a convergence semiangle of 30 mrad, a collection semiangle of 20 mrad, and a beam current of ~10 pA.[33−35] Scattered electrons were dispersed in a Nion Iris spectrometer at 2 meV/channel and the energy resolution [full width half-maximum of the zero loss peak (ZLP)] was approximately 16 meV. Point spectra had their ZLP maxima normalized to unity and their ZLP tail background subtracted.

RESULTS AND DISCUSSION

Figure 1 shows the set of Au nanorhombus assemblies used to build our understanding of plasmon coupling, beginning with a single oblong, kite-like rhombus monomer (Figure 1a,e), and ending in a five-pointed starlike pentamer (Figure 1d,h). This approach requires structures with low geometric tolerances in order to ensure that any measurable differences are due to particle interactions, not particle heterogeneity. The representative scanning electron microscopy (SEM) images (Figure 1a−d) of the as-fabricated nanorhombi and the high-angle annular dark-field (HAADF) images (Figure 1e−h) of the as-measured nanorhombi show good fidelity. This demonstrates that the samples underwent almost no degradation after fabrication. A minimal amount of corner rounding is observed. Each nanorhombus was designed to have a thickness of 20 nm with an edge length of 250 nm, yielding long and short axis lengths of 400 and 300 nm, respectively. A 20 nm gap distance was chosen as smaller gaps had slight inconsistencies.

The EEL point spectra (Figure 2a) of the nanorhombus monomer highlight the importance of understanding the spatial distribution of LSP resonance energies. The green and blue traces in Figure 2a represent the EEL spectra collected near the end of one of the long-axis and short-axis positions,
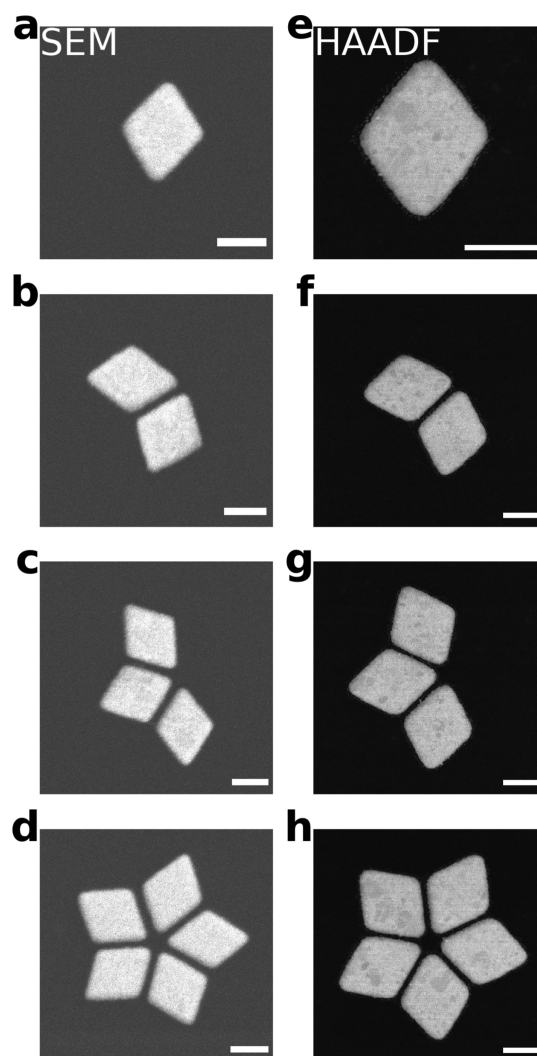

Figure 1. Postfabrication SEM images (a−d) show consistent fabrication across the sample. HAADF images of similar structures (e−h) taken at the time of measurements confirm the high fidelity of the fabricated nanorhombi. Scale bar corresponds to 200 nm.

respectively (see inset). Both point spectra show an identical peak labeled Q at 1250 meV. However, the two lower energy peaks in the spectra are clearly different, one occurring at 800 meV (L, green trace) and the other at 1000 meV (S, blue trace). Electron-driven discrete dipole approximation (e-DDA) simulations[36] were performed and the resulting e-DDA spectra (dashed) show similar peaks when the impact parameter is in the same position as the experimentally acquired data, set to be 10 nm away from the particle corners. The simulated nanorhombus was modeled with rounded corners to approximate the experimentally fabricated particles. All simulations of the nanorhombi were calculated in vacuum. The silicon nitride substrate present in the experiment has no resonances and is dispersionless in the energy range measured. Thus, the only effect the substrate will have on the nanorhombus is an overall red shift of the resonances because of the image effect, while in specific scenarios, the presence of a substrate causes non-negligible plasmonic interactions;[37−39] this is not the case for silicon nitride in this energy window. The thin silicon nitride substrate has a near-uniform refractive index of $n = 2.1$ in the studied energy range and will not cause any mode mixing or appreciable line width broadening.
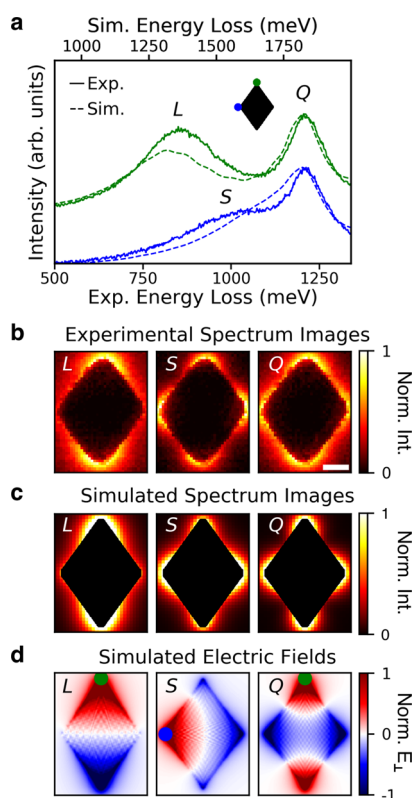
Figure 2. EEL point spectra (a), spectrum images (b,c), and simulated electric field maps (d) of an isolated nanorhombus show the three dominant lowest energy modes of the system: a long-axis dipole L, a short-axis dipole S, and a quadrupole Q. Experimental (solid, bottom x-axis) and full-wave electrodynamic simulations (dashed, top x-axis) of the EEL spectra are obtained at two different electron beam positions (as schematically shown by the colored circles in the inset). The intensity and energy loss of the simulated spectra have been rescaled (top x-axis) to account for substrate effects, which were not present in simulation. The calculated S peak (at ~1000 meV) is located at a higher energy than the experiment. Because the peak is broad and weak, it appears as a vague shoulder in the simulation and it is not as clearly resolved as in the experiment. Experimental (b) and simulated (c) spectrum images were taken by rastering the electron beam across the nanorhombus and collecting the energy lost at each point over a narrow energy window spanning the resonance. The scale bar size is 100 nm and the experimental spectrum image energy window is 100 meV (centered at the energy values denoted in each panel). The normal component of the electric fields (d) calculated at the three dominant resonances show the dipole/quadrupole orientations at each mode.

The identification of the LSP resonances is confirmed by collecting spectrum images at each peak (Figure 2b,c). In these measurements, the electron beam is rastered over the sample area, and an EEL spectrum is collected at each electron probe position. Each recorded spectrum is energy-aligned and normalized to the zero loss peak maximum; no further processing was performed (i.e., denoising). An energy window of 100 meV was used to obtain the spectrum images, which is approximately 5 times the energy resolution of the experiment and therefore sufficient to identify the individual LSP modes observed in this study. The experimental (Figure 2b) and simulated (Figure 2c) images show that the two lowest energy modes L and S are dipolar LSPs, and the higher energy mode Q is a quadrupolar LSP. It is clear then that the longer-axis dipole LSP is shifted lower in energy because of the elongated
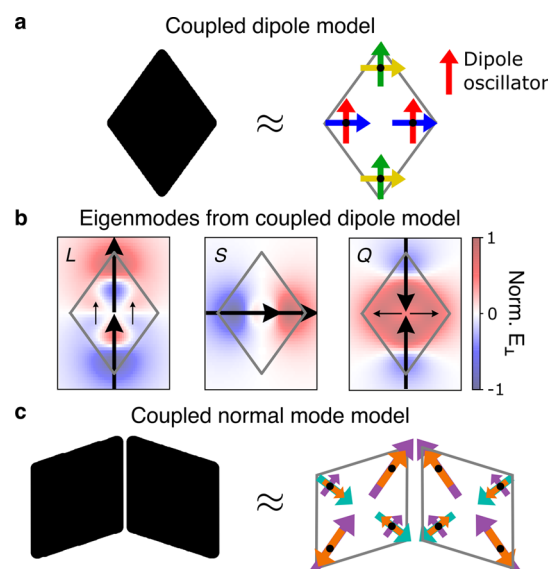

Figure 3. Illustration of the coupled dipole model (a,b) and coupled normal mode model (c) used to approximate the optical response of nanorhombus assemblies. The coupled dipole model (a) consists of eight unique dipole oscillators placed near the corners of the nanorhombi. The positions and polarizabilities of each dipole are determined by fitting the three lowest eigenmodes and eigenenergies of eq 1 to the simulated field maps, resonance frequencies, and damping rates of the long-axis dipole (L), short-axis dipole (S), and quadrupole (Q) in Figure 2. Each dipole with the same color is assigned the same polarizability. The resulting three lowest eigenmodes (b) are used to build the coupled normal mode model (c) where each nanorhombus is instead assigned three generalized oscillators, representing the three lowest energy modes (purple: long-axis dipole L, turquoise: short-axis dipole S, and orange: quadrupole Q). The overlayed electric field maps in (b) are the fields of the sphere dipoles evaluated in a plane parallel to and 60 nm above the dipoles.

shape (400 nm diameter vs 300 nm diameter). Simulated electric field maps (Figure 2d) of the normal component of the electric field evaluated on a plane parallel to and 4 nm above the surface of the nanorhombus further validate the identity of the modes. The electron beam positions that drive each mode are labeled on the maps. Note that the electric field map of the short-axis excitation in Figure 2d is not symmetric because the electron beam probe is driving a linear combination of both the short-axis dipole and quadrupole modes as they overlap spectrally (see Figure 2a).

A useful approach for understanding the hybridization schemes of coupled nanorhombi is to study the eigenmodes or normal modes of the assembly. Normal modes are independent of driving field, yet allow for the interpretation of peaks in the spectra. Numerical software for calculating eigenmodes exists;[40,41] however, we use a course-grained modeling scheme to reduce the dimensionality of the calculations. There are numerous reduced-order procedures for modeling coupled plasmonic nanoparticles.[42−45] The semianalytic approach presented here expands upon previous work[44,45] on cornered nanoparticles. Previous work demonstrated that the optical responses of such nanoparticles could be modeled with coupled dipoles localized at the corners of the nanoparticle. However, what the previous models do not account for is how to use this course-graining procedure to accurately quantify interparticle coupling. In this work, we use
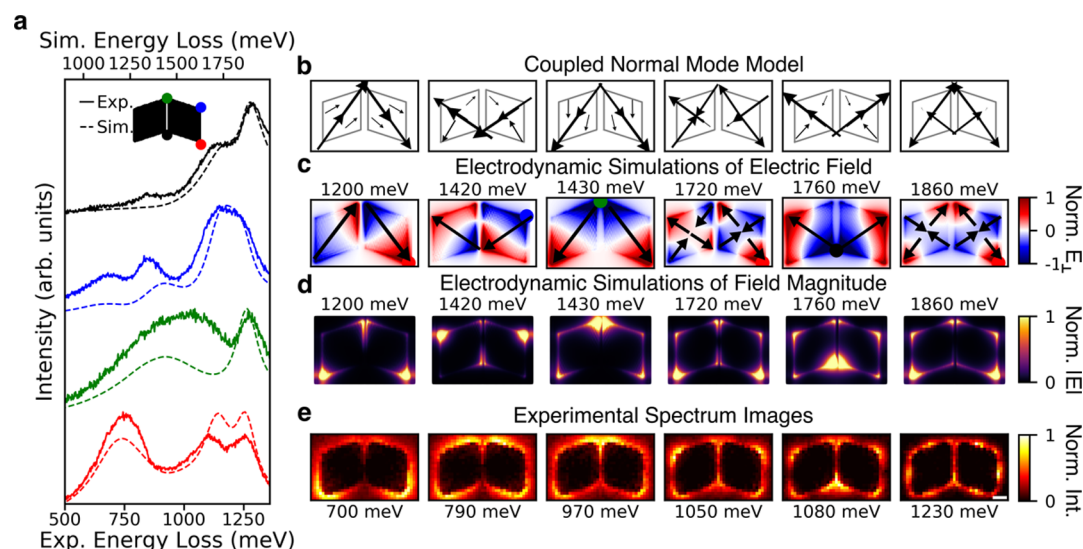
Figure 4. Simulated (dashed, top *x*-axis) and experimental (solid, bottom *x*-axis) EEL spectra (a) were taken at four different positions of a nanorhombus dimer as illustrated schematically by the colored circles in the inset. The coupled normal mode analysis procedure was used to predict the eigenmodes of the dimer (b) by approximating each rhombus as the three lowest energy modes predicted by the conventional coupled dipole theory. Simulated electric field maps (c) taken at the indicated beam positions and energies show all the six hybridized modes of the coupled nanorhombi that were predicted by the normal mode model. Arrows representing the total dipole moments from the field maps are overlaid on (c) to aid in the comparison with (b). An agreement between the predicted eigenmodes and the simulated field maps demonstrate the utility of the coupled normal mode model. The magnitude of the field maps (d) can be compared to the experimental spectrum images (e) to show that theory, simulation, and experiment are in agreement. The scale bar corresponds to 50 nm and the experimental spectrum image energy window is 100 meV (centered at the energy values denoted in each panel).

a similar course-grained modeling scheme to approximate the lowest energy modes of the rhombus monomer as generalized normal mode oscillators and use them to accurately describe the rhombus−rhombus coupling in different nanorhombus assemblies.

Using a single nanorhombus, we build the model by placing *x*-oriented and *y*-oriented dipole oscillators inside the four corners of a nanorhombus as shown in Figure 3a. Each symmetrically equivalent dipole oscillator is assigned a unique radius, which dictates its effective mass, damping rate, and resonance frequency.[46] All eight dipoles couple according to $g_{ij} = e^2\hat{q}_i \cdot \Lambda_{ij} \cdot \hat{q}_j$, where $\hat{q}_i$ is the unit vector of the *i*th dipole and $\Lambda_{ij} = [(3\hat{n}_{ij}\hat{n}_{ij} - 1)/r_{ij}^3 - ik/r_{ij}^2(3\hat{n}_{ij}\hat{n}_{ij} - 1) - k^2/r_{ij}(\hat{n}_{ij}\hat{n}_{ij} - 1)] e^{ir_{ij}k}$ is the dipole relay tensor, where r_{ij} is the distance between dipoles *i* and *j*, $\hat{n}_{ij}$ is the unit vector in the r_{ij} direction, and *k* is the wave vector. The coupled equations of motion become

$$m_i\ddot{q}_i + m_i\gamma_i\dot{q}_i + m_i\omega_{0i}^2q_i - \sum_{j \neq i}^{N} g_{ij}q_j = 0 \tag{1}$$

where $N = 8$ for the eight oscillators, q_i is the amplitude, m_i is the effective mass, γ_i is the radiative and nonradiative damping, and ω_{0i} is the resonance frequency of the *i*th oscillator. Solving eq 1 results in eight normal modes that can be used to predict all possible LSP resonances of the nanorhombus. By fitting the three lowest energy eigenmodes and eigenvalues of eq 1 to the simulated field maps (Figure 2d), resonance frequencies, and damping rates extracted from the simulated spectra, dipole positions and radii for the coupled dipole model are determined. These fits are accurate to within 30 meV of the simulated EEL spectra of the nanorhombus. The three predicted modes (*L*, *S*, and *Q*) are shown in Figure 3b, where the black arrows indicate the dipole orientations and magnitudes at the given energy and phase. The normal component of the electric fields produced by each dipole

oscillator is overlaid for ease in comparison to Figure 2d. An agreement between Figures 3b and 2d reflects the coupled dipole model and the fit parameters (radii and dipole positions) accurately account for the optical response of an individual nanorhombus.

However, the coupled dipole model will not suffice in modeling the rhombus−rhombus interactions primarily because the coupling among the corner-located dipoles on each nanorhombus will be overestimated. Instead, the dipole orientations, mode energies, and damping rates of the three lowest energy eigenmodes (*L*, *S*, and *Q*) from the coupled dipole model are used to parameterize generalized normal mode oscillators. This new model is depicted in Figure 3c, where each colored arrow corresponds to one of the normal modes (purple: long-axis dipolar LSP, turquoise: short-axis dipolar LSP, and orange: quadrupolar LSP). The equations of motion become

$$m\ddot{x}_\mu + m\gamma_\mu\dot{x}_\mu + m\omega_{0\mu}^2x_\mu - \sum_{\nu \neq \mu}\sum_{i,j}\frac{q_{\mu i}}{\bar{q}_\mu}g_{\mu i,\nu j}x_\nu = 0 \tag{2}$$

where the Greek indices refer to the generalized normal mode coordinates, and the Latin indices refer to the comprising corner-located dipoles. x_μ is the oscillator coordinate of one of the three normal modes on each particle, *m* is a geometric mass assigned to each normal mode, and $\omega_{0\mu}$ and γ_μ are the real and imaginary parts of the eigenvalue from the coupled dipole model. The pairwise coupling between the nanorhombi is defined by taking a weighted sum of the dipole−dipole coupling among all corner-located dipoles, where $\bar{q}_\mu = \sum_i q_{\mu i}/N$.

We demonstrate the efficacy of the model by comparing it to experimental and e-DDA simulated spectra, spectrum images, and field maps of a nanorhombus dimer. The EEL spectra acquired at four unique electron beam positions of the coupled
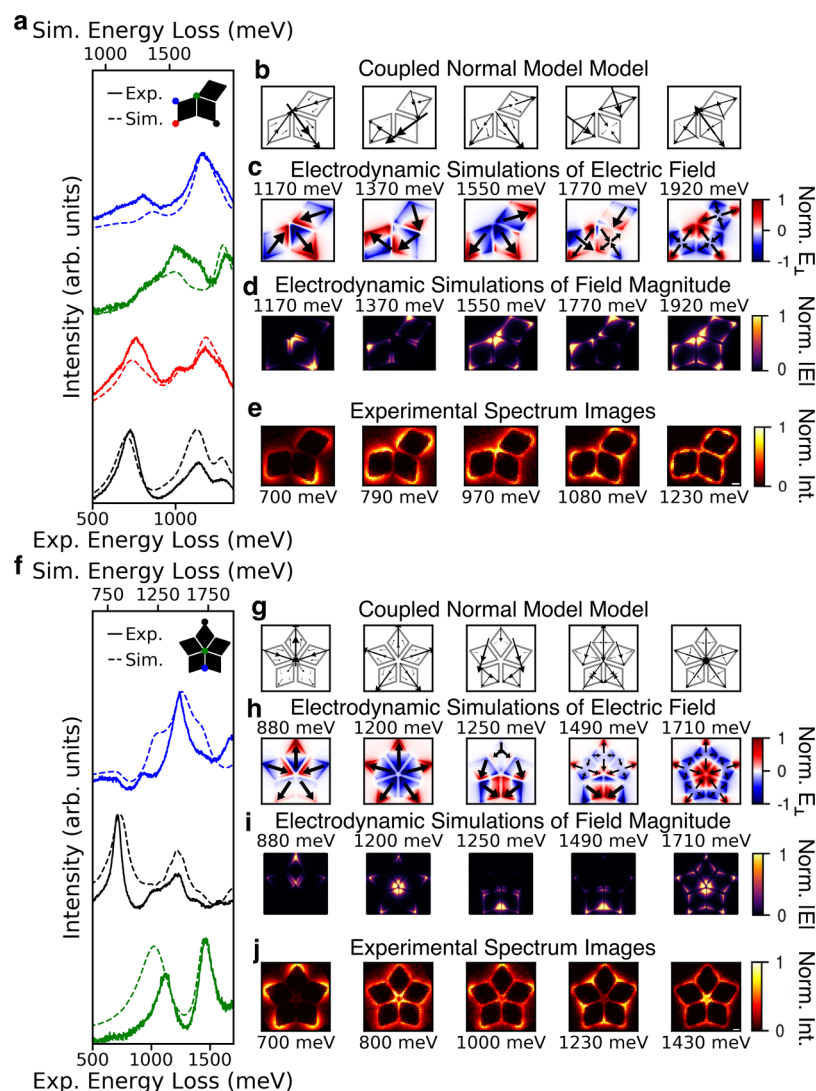
Figure 5. Normal mode analysis of the trimer (a−d) and pentamer (e−h) shows hybridization of the long-axis dipole, short-axis dipole, and quadrupole. (a,e) Simulated (dashed, top *x*-axis) and experimental (solid, bottom *x*-axis) spectra were collected at the beam positions labeled in the inset. Of the normal modes predicted by the coupled normal mode model, only the five shown in (b,f) can be resolved in the spectra. The simulated electric fields (c,g) exactly correspond to the predicted eigenmodes. The experimental spectrum images (d,h) were taken at the corresponding energies and the identities of the hybridized modes were further validated. The scale bar size is 50 nm, and the experimental spectrum image energy window is 100 meV (centered at the energy values denoted in each panel).

dimer are shown in Figure 4a. The spatial configuration of the six eigenmodes predicted by the analytic model is shown in Figure 4b. The normal modes have been vertically aligned with the corresponding simulated electric fields (Figure 4c,d) and experimental spectrum images (Figure 4e) taken at each resonance position. Arrows have been drawn on the simulated electric field maps to facilitate comparison between the simulated maps and the modes obtained from the analytical model. The agreement between the e-DDA simulations and experiment with the analytical model shown in Figure 4b−e demonstrates that the optical responses of the coupled nanorhombi system can be well described by the coupled normal mode model developed here.

The corroboration of the analytic model allows for the interpretation of the spectra in Figure 4a. The two lowest energy normal modes are the head-to-tail aligned hybridized long-axis dipoles (700 meV) and short-axis dipoles (790 meV). The dipoles are best driven when the electron beam is positioned on either corner of the outer edges of the

nanorhombus dimer, and they show up as the lowest energy peaks in the spectra (red and blue circles in the inset of Figure 4a). The complements of the long-axis and short-axis hybridized modes (tail-to-tail) are driven most strongly when the electron beam is located at the two corners of the edges shared by the two nanorhombi (green and black circles in the inset of Figure 4a). Last, the quadrupole hybridization is best observed when the electron beam is located at the outer corners of the longest axes (red spectra), with the two highest energy peaks showing the signature peak splitting of the head-to-tail and tail-to-tail modes.

The three-particle coupled nanorhombus assembly (Figure 5a−d) and a highly symmetric five-particle coupled assembly (Figure 5e−h) offer two additional systems to study the hybridization schemes. As with Figure 4, simulated and experimental point spectra were collected at different beam positions (labeled with colored circles in the inset). While the theoretical model predicts 9 possible normal modes for the trimer and 15 normal modes for the pentamer, only the 5

shown in each system are resolvable. The other normal modes are inaccessible because of the near degeneracy and spectral overlap within the energy resolution of the data. Nevertheless, a clear indication of the hybridization between the long-axis dipole LSP, short-axis dipole LSP, and quadruple LSP are observed. Once again, the point spectra as well as the spectrum images have LSP resonances that are highly sensitive to the host geometry and near-field coupling behavior.

A subset of the predicted normal modes (Figure 5b,g) are aligned with the simulated electric field maps (Figure 5c,d,h,i) and experimental spectrum images (Figure 5e,j) of each resonance. Similar to the dimer, the three lowest energy modes of the trimer, as measured experimentally, are the head-to-tail long-axis (700 meV), head-to-tail short-axis (790 meV), and tail-to-tail long-axis (970 meV) hybridized modes. However, contrary to the dimer, the next energy mode (1080 meV) is not clearly an all-long axis, all-short axis, or all-quadrupole hybridization scheme. Instead, it is a mixture of the short-axis and quadruple modes and is accessible at all electron beam positions. The field profiles on each nanorhombus are also mixing between the short-axis and quadrupole orientations. Furthermore, while the tail-to-tail quadrupole clearly exists (1230 meV), the head-to-tail hybridization appears as a predicted normal mode but does not arise as an isolated feature in the spectra. This is due to the spectral overlap of the all-quadrupole and quadrupole—quadrupole—short-axis modes, where the latter mode dominates.

Similar to the trimer, the pentamer also supports five resolvable normal modes that were predicted by the analytic model. The two lowest energy modes, as measured experimentally, are the long-axis dipole hybridized into the head-to-tail (700 meV) and all tail-to-tail (800 meV) arrangements. In this case, there are not any observable all short-axis dipole modes and instead only combinations arising from short-axis dipole—quadrupole coupling. Similar to the trimer, however, the analytic model does predict a head-to-tail all-short-axis mode arrangement, but it is again not resolvable because of the overlap of the third mode presented here. Last, the all-quadrupole tail-to-tail mode is once again present (1430 meV) and easily excitable when the electron beam is positioned at the center of the pentamer.

CONCLUSIONS

In conclusion, our work demonstrates the ability to precisely nanofabricate nanorhombus assemblies, characterize their plasmonic properties, and model the interparticle coupling across a variety of arrangements. As we build from a monomer to a pentamer, the experimental and simulated point spectra, spectrum images, and near-field maps agree well with the coupled normal mode model developed here. We observe that the infrared optical responses of coupled nanorhombus systems can be explained by coupling among the nanorhombus' two dipolar and one quadrupolar LSP modes. By examining these different assemblies, we see that the head-to-tail arrangement of the long-axis dipoles always yields the lowest energy hybrid peak observed in the spectra. Therefore, we predict that examining low-energy hybrid modes across heterogeneous nanorhombus structures can be greatly simplified by measuring along this axis. Similarly, the all-quadrupole tail-to-tail modes lie higher in energy and are easily excitable and resolvable at the same probe positions. However, in the mid-range energy window, the short-axis dipole and the

quadrupole LSPs mix on the particles themselves and across the hybridized normal mode itself.

The simple coupled normal mode model presented here is able to quantitatively predict the plasmon modes of the nanorhombus across a wide range of energies and spatial distributions. We expect that the model will help further guide experiments and data analysis even when examining larger and more extended nanorhombus assemblies. Additionally, the analytical model can be reparameterized with different monomer sizes and shapes to quickly predict the normal modes and energies of other coupled systems. This offers the ability to easily explore the plasmonic responses of many other corner-dominated nanoparticle arrangements. Although in this work we studied the near-field coupling and hybridization effects of cornered nanoparticle clusters, the approach shown here can furthermore be applied to study the role of short-intermediate-, and far-field coupling effects in extended plasmonic assemblies.

AUTHOR INFORMATION

Corresponding Author

Juan Carlos Idrobo − *Center for Nanophase Materials Sciences, Oak Ridge National Laboratory, Oak Ridge, Tennessee 37831, United States;* orcid.org/0000-0001-7483-9034; Email: idrobojc@ornl.gov

Authors

Claire A. West − *Department of Chemistry, University of Washington, Seattle, Washington 98195, United States;* orcid.org/0000-0001-8921-5275

Agust Olafsson − *Department of Chemistry and Biochemistry, University of Notre Dame, Notre Dame, Indiana 46556, United States;* orcid.org/0000-0001-5252-7881

Grace Pakeltis − *Department of Materials Science and Engineering, University of Tennessee, Knoxville, Tennessee 37996, United States;* orcid.org/0000-0003-1478-4654

David A. Garfinkel − *Department of Materials Science and Engineering, University of Tennessee, Knoxville, Tennessee 37996, United States;* orcid.org/0000-0002-7593-1868

Philip D. Rack − *Department of Materials Science and Engineering, University of Tennessee, Knoxville, Tennessee 37996, United States; Center for Nanophase Materials Sciences, Oak Ridge National Laboratory, Oak Ridge, Tennessee 37831, United States;* orcid.org/0000-0002-9964-3254

David J. Masiello − *Department of Chemistry, University of Washington, Seattle, Washington 98195, United States;* orcid.org/0000-0002-1187-0920

Jon P. Camden − *Department of Chemistry and Biochemistry, University of Notre Dame, Notre Dame, Indiana 46556, United States;* orcid.org/0000-0002-6179-2692

Complete contact information is available at:
https://pubs.acs.org/10.1021/acs.jpcc.0c08098

Author Contributions

⊥C.A.W. and A.O. contributed equally.

Notes

The authors declare no competing financial interest.

■ REFERENCES

(1) Brandl, D. W.; Mirin, N. A.; Nordlander, P. Plasmon modes of nanosphere trimers and quadrumers. *J. Phys. Chem. B* **2006**, *110*, 12302−12310.

(2) Bao, K.; Mirin, N. A.; Nordlander, P. Fano resonances in planar silver nanosphere clusters. *Appl. Phys. A* **2010**, *100*, 333−339.

(3) Yang, Z.-J.; Zhang, Z.-S.; Zhang, W.; Hao, Z.-H.; Wang, Q.-Q. Twinned Fano interferences induced by hybridized plasmons in Au−Ag nanorod heterodimers. *Appl. Phys. Lett.* **2010**, *96*, 131113.

(4) Yan, B.; Boriskina, S. V.; Reinhard, B. M. Optimizing gold nanoparticle cluster configurations (n ≤ 7) for array applications. *J. Phys. Chem. C* **2011**, *115*, 4578−4583.

(5) Maier, S. A. *Plasmonics: Fundamentals and Applications*; Springer Science & Business Media, 2007.

(6) Bohren, C. F.; Huffman, D. R. *Absorption and Scattering of Light by Small Particles*; John Wiley & Sons, 2008.

(7) Nehl, C. L.; Hafner, J. H. Shape-dependent plasmon resonances of gold nanoparticles. *J. Mater. Chem.* **2008**, *18*, 2415−2419.

(8) Dregely, D.; Hentschel, M.; Giessen, H. Excitation and tuning of higher-order Fano resonances in plasmonic oligomer clusters. *ACS Nano* **2011**, *5*, 8202−8211.

(9) Nordlander, P.; Prodan, E. Plasmon hybridization in nanoparticles near metallic surfaces. *Nano Lett.* **2004**, *4*, 2209−2213.

(10) Wang, Y.; Li, Z.; Zhao, K.; Sobhani, A.; Zhu, X.; Fang, Z.; Halas, N. J. Substrate-mediated charge transfer plasmons in simple and complex nanoparticle clusters. *Nanoscale* **2013**, *5*, 9897−9901.

(11) Grady, N. K.; Halas, N. J.; Nordlander, P. Influence of dielectric function properties on the optical response of plasmon resonant metallic nanoparticles. *Chem. Phys. Lett.* **2004**, *399*, 167−171.

(12) Miller, M. M.; Lazarides, A. A. Sensitivity of metal nanoparticle surface plasmon resonance to the dielectric environment. *J. Phys. Chem. B* **2005**, *109*, 21556−21565.

(13) Stiles, P. L.; Dieringer, J. A.; Shah, N. C.; Van Duyne, R. P. Surface-enhanced Raman spectroscopy. *Annu. Rev. Anal. Chem.* **2008**, *1*, 601−626.

(14) Sreekanth, K. V.; Alapan, Y.; ElKabbash, M.; Ilker, E.; Hinczewski, M.; Gurkan, U. A.; De Luca, A.; Strangi, G. Extreme sensitivity biosensing platform based on hyperbolic metamaterials. *Nat. Mater.* **2016**, *15*, 621−627.

(15) Schädle, T.; Mizaikoff, B. Mid-infrared waveguides: a perspective. *Appl. Spectrosc.* **2016**, *70*, 1625−1638.

(16) Adleman, J. R.; Boyd, D. A.; Goodwin, D. G.; Psaltis, D. Heterogenous catalysis mediated by plasmon heating. *Nano Lett.* **2009**, *9*, 4417−4423.

(17) Guo, J.; Zhang, Y.; Shi, L.; Zhu, Y.; Mideksa, M. F.; Hou, K.; Zhao, W.; Wang, D.; Zhao, M.; Zhang, X.; et al. Boosting hot electrons in hetero-superstructures for plasmon-enhanced catalysis. *J. Am. Chem. Soc.* **2017**, *139*, 17964−17972.

(18) Clavero, C. Plasmon-induced hot-electron generation at nanoparticle/metal-oxide interfaces for photovoltaic and photocatalytic devices. *Nat. Photonics* **2014**, *8*, 95.

(19) Zada, A.; Muhammad, P.; Ahmad, W.; Hussain, Z.; Ali, S.; Khan, M.; Khan, Q.; Maqbool, M. Surface plasmonic-assisted photocatalysis and optoelectronic devices with noble metal nanocrystals: design, synthesis, and applications. *Adv. Funct. Mater.* **2020**, *30*, 1906744.

(20) Link, S.; El-Sayed, M. A. Size and temperature dependence of the plasmon absorption of colloidal gold nanoparticles. *J. Phys. Chem. B* **1999**, *103*, 4212−4217.

(21) Jin, R.; Cao, Y.; Mirkin, C. A.; Kelly, K. L.; Schatz, G. C.; Zheng, J. Photoinduced conversion of silver nanospheres to nanoprisms. *Science* **2001**, *294*, 1901−1903.

(22) Jain, P. K.; Huang, W.; El-Sayed, M. A. On the universal scaling behavior of the distance decay of plasmon coupling in metal nanoparticle pairs: a plasmon ruler equation. *Nano Lett.* **2007**, *7*, 2080−2088.

(23) Tabor, C.; Van Haute, D.; El-Sayed, M. A. Effect of orientation on plasmonic coupling between gold nanorods. *ACS Nano* **2009**, *3*, 3670−3678.

(24) Funston, A. M.; Novo, C.; Davis, T. J.; Mulvaney, P. Plasmon coupling of gold nanorods at short distances and in different geometries. *Nano Lett.* **2009**, *9*, 1651−1658.

(25) Zhao, L.; Kelly, K. L.; Schatz, G. C. The extinction spectra of silver nanoparticle arrays: influence of array structure on plasmon resonance wavelength and width. *J. Phys. Chem. B* **2003**, *107*, 7343−7350.

(26) Ringe, E.; McMahon, J. M.; Sohn, K.; Cobley, C.; Xia, Y.; Huang, J.; Schatz, G. C.; Marks, L. D.; Van Duyne, R. P. Unraveling the effects of size, composition, and substrate on the localized surface plasmon resonance frequencies of gold and silver nanocubes: a systematic single-particle approach. *J. Phys. Chem. C* **2010**, *114*, 12511−12516.

(27) Keilmann, F.; Hillenbrand, R. Near-field microscopy by elastic light scattering from a tip. *Philos. Trans. R. Soc., A* **2004**, *362*, 787−805.

(28) Hutter, E.; Fendler, J. H. Exploitation of localized surface plasmon resonance. *Adv. Mater.* **2004**, *16*, 1685−1706.

(29) Zayats, A. V.; Smolyaninov, I. I.; Maradudin, A. A. Nano-optics of surface plasmon polaritons. *Phys. Rep.* **2005**, *408*, 131−314.

(30) Kociak, M.; Stéphan, O. Mapping plasmons at the nanometer scale in an electron microscope. *Chem. Soc. Rev.* **2014**, *43*, 3865−3883.

(31) Wu, Y.; Li, G.; Camden, J. P. Probing nanoparticle plasmons with electron energy loss spectroscopy. *Chem. Rev.* **2017**, *118*, 2994−3031.

(32) Cherqui, C.; Thakkar, N.; Li, G.; Camden, J. P.; Masiello, D. J. Characterizing localized surface plasmons using electron energy-loss spectroscopy. *Annu. Rev. Phys. Chem.* **2016**, *67*, 331−357.

(33) Krivanek, O. L.; Lovejoy, T. C.; Dellby, N.; Aoki, T.; Carpenter, R. W.; Rez, P.; Soignard, E.; Zhu, J.; Batson, P. E.; Lagos, M. J.; et al. Vibrational spectroscopy in the electron microscope. *Nature* **2014**, *514*, 209−212.

(34) Hachtel, J. A.; Lupini, A. R.; Idrobo, J. C. Exploring the capabilities of monochromated electron energy loss spectroscopy in the infrared regime. *Sci. Rep.* **2018**, *8*, 5637.

(35) Lovejoy, T. C.; Corbin, G. C.; Dellby, N.; Hoffman, M. V.; Krivanek, O. L. Advances in ultra-high energy resolution STEM-EELS. *Microsc. Microanal.* **2018**, *24*, 446−447.

(36) Bigelow, N. W.; Vaschillo, A.; Iberi, V.; Camden, J. P.; Masiello, D. J. Characterization of the electron- and photon-driven plasmonic excitations of metal nanorods. *ACS Nano* **2012**, *6*, 7497−7504.

(37) Cherqui, C.; Li, G.; Busche, J. A.; Quillin, S. C.; Camden, J. P.; Masiello, D. J. Multipolar nanocube plasmon mode-mixing in finite substrates. *J. Phys. Chem. Lett.* **2018**, *9*, 504−512.

(38) Li, G.; Cherqui, C.; Bigelow, N. W.; Duscher, G.; Straney, P. J.; Millstone, J. E.; Masiello, D. J.; Camden, J. P. Spatially mapping energy transfer from single plasmonic particles to semiconductor substrates via STEM/EELS. *Nano Lett.* **2015**, *15*, 3465−3471.

(39) Wu, Y.; Li, G.; Cherqui, C.; Bigelow, N. W.; Thakkar, N.; Masiello, D. J.; Camden, J. P.; Rack, P. D. Electron energy loss spectroscopy study of the full plasmonic spectrum of self-assembled AuAg alloy nanoparticles: unraveling size, composition, and substrate effects. *ACS Photonics* **2016**, *3*, 130−138.

(40) Oskooi, A. F.; Roundy, D.; Ibanescu, M.; Bermel, P.; Joannopoulos, J. D.; Johnson, S. G. MEEP: A flexible free-software package for electromagnetic simulations by the FDTD method. *Comput. Phys. Commun.* **2010**, *181*, 687−702.

(41) Hohenester, U.; Trügler, A. MNPBEM—A Matlab toolbox for the simulation of plasmonic nanoparticles. *Comput. Phys. Commun.* **2012**, *183*, 370−381.

(42) Salary, M. M.; Forouzmand, A.; Mosallaei, H. Model order reduction of large-scale metasurfaces using a hierarchical dipole approximation. *ACS Photonics* **2017**, *4*, 63−75.

(43) Tajdini, M. M.; Mosallaei, H. Characterization of large array of plasmonic nanoparticles on layered substrate: dipole mode analysis integrated with complex image method. *Opt. Express* **2011**, *19*, A173−A193.

(44) Griffin, S.; Montoni, N. P.; Li, G.; Straney, P. J.; Millstone, J. E.; Masiello, D. J.; Camden, J. P. Imaging energy transfer in Pt-decorated Au nanoprisms via electron energy-loss spectroscopy. *J. Phys. Chem. Lett.* **2016**, *7*, 3825−3832.

(45) Rodríguez-Fernández, J.; Novo, C.; Myroshnychenko, V.; Funston, A. M.; Sánchez-Iglesias, A.; Pastoriza-Santos, I.; Pérez-Juste, J.; García de Abajo, F. J.; Liz-Marzán, L. M.; Mulvaney, P. Spectroscopy, imaging, and modeling of individual gold decahedra. *J. Phys. Chem. C* **2009**, *113*, 18623−18631.

(46) Moroz, A. Depolarization field of spheroidal particles. *J. Opt. Soc. Am. B* **2009**, *26*, 517−527.